

For refereed journal publication, 1996

Diurnal thermal cycling effects on backscatter of thin sea ice

S. V. Nghiem, R. Kwok, and S. H. Yueh
Center for Space Microelectronics Technology
Jet Propulsion Laboratory, California Institute of Technology
Pasadena, California

A. J. Gow and D. K. Perovich
U.S. Army Cold Regions Research and Engineering Laboratory
Hanover, New Hampshire

C. C. Hsu, K. H. Ding, and J. A. Kong
Department of Electrical Engineering and Computer Science
and Research Laboratory of Electronics
Massachusetts Institute of Technology
Cambridge, Massachusetts

T. C. Grenfell
Department of Atmospheric Sciences
University of Washington
Seattle, Washington

Mail: JPL, MS 300-235, 4800 Oak Grove Dr., Pasadena, CA 91109
ngkiem@malibu.jpl.nasa.gov; Tel 81 8-354-2982; Fax 818-393-5285

Diurnal thermal cycling effects on backscatter of thin sea ice

S. V. Nghiem, R. Kwok, and S. J. Yeh

Center for Space Microelectronics Technology

Jet Propulsion Laboratory, California Institute of Technology

Pasadena, California

A. J. Gow and D. K. Perovich

U.S. Army Cold Regions Research and Engineering Laboratory

Hanover, New Hampshire

C. C. Hsu, K. H. Ding, and J. A. Kong

Department of Electrical Engineering and Computer Science and

Research Laboratory of Electronics, Massachusetts Institute of Technology

Cambridge, Massachusetts

T. C. Grenfell

Department of Atmospheric Sciences

University of Washington

Seattle, Washington

Abstract. To investigate effects on polarimetric backscatter of sea ice grown under diurnal cycling conditions, we carried out an experiment in January 1994 at the outdoor Geophysical Research Facility in the Cold Regions Research and Engineering Laboratory. The ice sheet grew from open sea water to a thickness of 10 cm in 2.5 days, during which we took polarimetric backscatter data with a C-band scatterometer in conjunction with meteorological, sea ice characterization, and microwave emission measurements. The initial ice growth in the late morning of 19 January 1994 was slow due to high insolation. As the air temperature dropped during the night, the growth rate increased significantly. Air temperature changed drastically from about -12°C to -36°C between day and night. The diurnal thermal cycle repeated in the next day and the growth rate varied in the same manner. Ice temperature profiles clearly show the diurnal cycling response in the ice sheet with a lag of 2.5 hours behind the time of maximum short-wave incident solar radiation. Measured sea ice backscatter reveals substantial diurnal variations up to 6 dB with repeatable cycles in sync with the temperature cycles and the emission modulations. A diurnal backscatter model based on sea ice electrodynamics and thermodynamics explains the diurnal signature with good comparisons between theoretical and experimental results. This work shows that diurnal effects are imperative to inversion algorithms for retrieving sea ice geophysical parameter from remote sensing satellite SAR and scatterometer data.

1. Introduction

Leads containing thin ice in the perennial sea ice pack significantly contribute to the heat transfer between the Arctic Ocean and the atmosphere. By triggering fog and clouds, leads strongly disturb the net radiative transfer balance [Ruffieux *et al.*, 1995]. Leads impact the thermohaline structure of the upper Arctic Ocean despite of their small areal coverage relative to other sea ice types. In active leads, salt released by rapid freezing mixes downward by turbulence [McPhee and Stanton, 1996]. From the Leads Experiment in March and April 1992 on the Arctic ice cap about 200 km north of Prudhoe bay [LeadEx Group, 1993], Ruffieux *et al.* [1995] found that the sun was effective in reducing the surface freezing rate of lead ice formation and in halting the convective mixing in the ocean under the leads. They concluded that downward short-wave radiation was responsible for driving the diurnal cycles [Ruffieux *et al.*, 1995]. From the same experiment, McPhee and Stanton [1996] observed large downward oceanic heat flux near solar noon in the diurnal cycle of warming and cooling of the mixed layer.

With spaceborne infrared images under the cloud-free condition, Ikeda [1989] demonstrated the diurnal effect on sea ice, which appears brighter in nighttime images than in daytime images. Using airborne X-band Synthetic Aperture Radar (SAR) images, Barber *et al.* [1992] reported diurnal differences in multi-year ice and in a rubble field seen at two different times in the Canadian Arctic Archipelago. These results, however, did not include diurnal observations of thin sea ice in active leads. Moreover, the disadvantage of using satellite data to investigate diurnal signature of sea ice in remote sensing data and their relation to diurnal responses in sea ice physical properties is sparse observations in

time [Ikeda, 1989]. Yet understanding the physical mechanisms responsible for observed diurnal signatures is imperative to correctly interpret and retrieve geophysical parameters from remote sensing data.

The objective of the present work is to investigate the diurnal signature in C-band polarimetric backscatter of thin sea ice in active leads. Furthermore, we study the linkage between the diurnal backscatter signature and sea ice physical properties undergoing cooling and warming cycles driven by insolation. An important implication of the results in this paper is that diurnal effects need to be considered in the retrieval of geophysical parameters such as sea ice thickness. The C-band polarimetric results are of particular interest since many present and near future spaceborne SARs and scatterometers such as ERS-1, ERS-2, ENVISAT, RADARSAT, and RADARSAT-2 operate at C band with different polarizations.

In this paper, we present observations on C-band polarimetric backscatter of sea ice growing under diurnal cycling conditions. We conducted the experiment at the outdoor Geophysical Research Facility (GRF) in the Cold Regions Research and Engineering Laboratory (CRREL) from 19 to 21 January 1994, during which the ice sheet grew to a thickness of 10 cm. This thickness was in the same range of the diurnal study by Ruffieux et al. [1995] in LeadEx, which emphasized leads covered with thin ice during the first few days of their life cycles. The meteorological environment in the 1994 winter time of our experiment at CRREL was particularly suitable for the diurnal study since the air temperature plunged down to the cold Arctic condition ($\sim 36^{\circ}\text{C}$), the temperature changed more than 20°C between day and night, and the mostly clear sky allowed good insolation. We used the Jet Propulsion Laboratory (JPL) scatterometer to take polarimetric

data in conjunction with meteorological, sea ice characterization, and microwave emission measurements.

The paper consists of four sections. Section 2 discusses the experimental facility, setup, and data collection. Section 3 presents the environmental conditions, sea ice growth process, and physical characteristics. Section 4 shows the observed diurnal signature in sea ice backscatter, relates the signature to sea ice physical properties, and explains the observation with a diurnal backscatter model. Finally, Section 5 summarizes the main conclusions of the paper.

2. Experimentation

2.1. Facility

The ice sheet grew in the G R F pool filled with sea water. The pool was 18.3-111 long, 7.62-111 wide, and 2.14-111 deep as shown in Figure 1. At one end of the pool was a reservoir to hold excess ice or snow clean up from the pool surrounding. A gantry, with two horizontal 1 beams about 4 m above the surface of the ice sheet, was movable on rails along the pool. The gantry provided the support to mount the Jet Propulsion Laboratory (JPL) polarimetric scatterometer. A tent at a corner of the pool housed the scatterometer controller, computer, and operators. Several power sources were available in the tent and heaters kept the tent warmed. At the other corner on the same side of the pool (see Figure 1), there was a small pump house where the controlling computer for acquiring temperature profiles of the ice sheet located. A cement walkway connected the tent and the pump house, where we setup a site for calibration targets.

For environmental conditions, CRREL used a meteorological station to measure short-wave and long-wave radiation, air temperature, wind speed and direction at 4-m height, and other parameters [*U. S. Army TECOM Hanover Meteorological Team, 1994*]. For sea ice characterization, CRREL had an indoor refrigerated room in the Ice Engineering Facility for preparing sea ice samples to study crystallographic structures. Gow and Week [1977] and Gow et al. [1987] described the technique using a histological microtome to obtain horizontal and vertical thin sections from samples for a three-dimensional view of sea ice structure. Two thermistor strings emerged in sea water at the beginning of the sea ice growth gave temperature profiles of sea ice and sea water as a function of time during the experiment. The University of Washington (UW) had a radiometer suite [*Grenfell and Lohanick, 1985*] to measure natural microwave emissions from the ice sheet.

2.2. Experimental Setup

Figure 2 shows the scatterometer antenna with the positioner mounted on the gantry I beams. The antenna was a dual polarization diagonal horn installed on a square frame, which we rotated around a horizontal axis with a remote-controlled motor to set the incident angle. In Figure 2, the antenna was at the position of normal incidence or 0° incident angle. The entire antenna fixture was bolted on a ball bearing disk driven with another remote controlled motor to change the azimuth angle. This setup allowed the pointing of the antenna to any arbitrary incident and azimuth angles.

The insulated white box seen in the photo contains RF electronic components, which are constantly kept at the room temperature of 25°C throughout the experiment. Periodically, we checked the internal controlled temperature displayed through a small rectangular

window seen on the front panel of the RF box in Figure 2.. We achieved a very stable temperature inside the RF box using an electric fan and a heater controlled by an internal temperature processor. The scatterometer computer and controllers together with the network analyzer were in the tent, from which we operated the scatterometer and took polarimetric backscatter data. The scatterometer was a step-frequency radar with the center frequency of 5 GHz, a bandwidth of 1 GHz, and a beamwidth of 12° . The scatterometer system, antenna characteristics, operation, sensitivity, calibration, and data processor have been presented elsewhere [Nghiem, 1993; Nghiem et al., 1996b] .

For this experiment, we arranged calibration targets on a Styrofoam pedestal placed on top of a cardboard box at the calibration site indicated in Figure 1. The calibration targets were a trihedral corner reflector and a metallic sphere. We covered the front of the box and the background of the calibration target with microwave absorber sheets to reduce the noise. The coherent subtraction technique was applied to obtain excellent calibration data. We regularly made clear sky measurements to determine system noises for removal from calibration and sea ice measurements.

The CRREL meteorological station situated on an elevated terrain about 7.3 m above and 183 m away from the GRF pond. We also took sea ice samples before each set of backscatter data acquisition to measure ice thickness, salinity, and structure. The thermistor strings stood vertically in the GRF pool at a place in front of the pump house and away from scatterometer footprints for all incident and azimuth angles. To verify the uniformity of temperatures, we used a hand-held digital thermometer to take air and ice surface temperatures at the other end of the pool.

The UW sensors included a 90- GHz radiometer located on the side of the pool across

from the scatterometer calibration site as illustrate in Figure 1. The radiometer was a noise-injection type with a bandwidth of 500 MHz and a field-of-view of 6° from a horn lens antenna. This radiometer was suit able for surface-based measurements of sea ice in Arctic field conditions [*Grenfell and Lohanick, 1985*]. The height of the radiometer antenna was approximately 1.5 m above the surface of the ice sheet.

2.3. Data Collection

For approximately every 1 cm of the ice growth, we took a set of polarimetric backscatter data. The range of incident angles was from 0.0° to 60° with an increment of 5° . At every incident angle, we measured full scattering matrices for three independent azimuth angles. Each scattering matrix was a coherent average of 20 samples with 401 frequency points over 1 GHz bandwidth. The data processing [*Nghiem, 1993; Nghiem et al., 1996b*] included data decompression, system noise removal, windowing, Fourier transforms, time gating, system transfer function computation, signal reconstruction, ensemble averaging, three-dimensional antenna pattern characterization, backscatter deconvolution, polarimetric calibration, and radiometric calibration. Processed backscatter data consist of σ_{hh} for horizontal polarization, σ_{vv} for vertical polarization, σ_{hv} for cross-polarization, and ρ for complex correlation between horizontal and vertical returns. Copolarized and cross-polarized fields are not correlated due to the azimuthal symmetry of the ice sheet.

The meteorological station for environmental monitoring at CRREL had sensors for air temperature, radiation at short and long waves, wind speed, and wind direction. For air temperature, Rotronics MP-100 Probe took data and averaged measurements over 15 minutes with an accuracy of 0.1°C . The sensors for radiation were short-wave ($0.3\text{-}3\text{ }\mu\text{m}$)

Qualimetrics 3020 Stappyradiometer and long-wave (3-50 μm) Hippely Pyrgometer. The wind monitor was RM Young 5103 for both wind speed and wind direction. The time tag for all data was local Julian day for every 15 minutes. The CRRRL Meteorological Team reported further information on the sensors and data collection [U. S. Army *TECOM Hanover Meteorological Team, 1994*].

We used two thermistor strings to monitor the vertical profile of temperature within the ice sheet, as well as air temperature above the ice and water temperature beneath the ice. The strings consisted of YSI-44033 precision thermistors mounted in solid 3.2-cm-diameter PVC rods. The spacing of the thermistors was every 0.5 cm in the top 7 cm below the air-ice interface, every cm from 7 to 18 cm and every 5 cm from 18 to 48 cm. A Campbell Scientific data logger recorded temperature profile data every 5 minutes. The thermistors had an absolute accuracy of 0.1°C and a sensitivity of approximately 0.03°C.

We took a set of radiometer and a set of scatterometer measurements separately in time and repeated this procedure for every growth stage. This interlacing arrangement between passive and active data acquisitions prevented interferences in microwave emission results. The time response of the ice sheet characteristics to environmental conditions was much slower compared to the time interval between the interlaced measurements. Hence, sea ice properties were similar between the radiometer and scatterometer observations for the same growth stage. Brightness temperatures of natural emission from the ice sheet for both horizontal and vertical polarizations considered in this paper were at 50° incident angle. The brightness accuracy was 2 K with a sensitivity of 0.5 K.

3. Sea Ice Growth

3.1. Environments

In midlatitude winter, the amplitude of solar radiation diurnal cycle is similar to the Arctic condition in late winter to early spring, such as the LeadEx March-April time [Ruffieux *et al.*, 1995]. The peak incident short-wave radiation is well above $400 \text{ W} \cdot \text{m}^{-2}$ at solar noon. This strong insolation drives the diurnal thermal cycling which forces physical changes in properties of sea ice. Figure 3a shows the incident radiation for both short (0.3 to $3 \mu\text{m}$) and long waves (3 to $50 \mu\text{m}$) measured by the meteorological station from 19 to 20 January 1994. The short-wave peak occurred close to local noon time and the amplitude was typically observed at the local midlatitude during winter. On the 21, some cloud cover reduced the downward short-wave amplitude. The long-wave radiation was between 200 to $300 \text{ W} \cdot \text{m}^{-2}$ with afternoon peaks lagging the short-wave peaks. Note that a small dip took place at noon on both 19 and 20 January; this midday cooling was also observed in the long-wave radiation at the LeadEx Arctic field [Ruffieux *et al.*, 1995].

The air temperature also lagged the incident short-wave radiation as seen in Figure 3b. Temperature measured by the station was close to the air temperature measured at GRF pond. The delay in the temperature peak was approximately 2.5 hours from the short-wave peak. Figure 3 indicates that the solar heating caused the steep slope in the temperature curve during noon time. As the sun went down, the temperature gradually cool down into the night until the next morning. The important results shown in the temperature plots is that the air temperature cooled down to -36°C , which is similar to the Arctic cold winter condition. In the winter of 1994, New Hampshire suffered one of the

coldest weather. Moreover, the temperature plunged more than 20°C from day to night. Arctic measurements in late winter also show a substantial heating during the day and cooling during the night [Ruffieux *et al.*, 1995].

An important factor in the study of diurnal effects is wind conditions. High winds significantly affect the surface heat convection and thus the ice growth [Adams *et al.*, 1991]. It is necessary to have a persistent or low wind condition to avoid complicated variations in the ice growth process. Over the duration of our experiment, the average wind speed measured at the meteorological station was only $0.6\text{ m}\cdot\text{s}^{-1}$ at 4-m height above the station ground level in addition to 7.3 m above the GRF pond. Since the GRF pond was in the middle of a low terrain surrounded by elevated hill sides, buildings, and fences, wind speeds at the experiment site were even lower or close to the still air condition. These environmental conditions encountered during this experiment are particularly suitable to study the diurnal backscatter signature of thin ice similar to the sea ice formation in Arctic leads.

3.2. Growth Process

We initiated the sea ice growth from open sea water at about 10:00 am local time on 1119 January 1994. The sea water had a salt mixture of mainly sodium chloride (NaCl), magnesium chloride (MgCl_2), magnesium sulfate (MgSO_4), calcium sulfate (CaSO_4), potassium sulfate (K_2SO_4), and calcium carbonate (CaCO_3). Table 1 lists the salt composition, chemical representation, and mixing portion used in this experiment to obtain a salinity of 30‰ , which is in the typical range of sea water salinity in the Arctic Ocean. This mixture contains the same salt fractions as in typical sea water [Neumann and Pierson,

1966] excluding traces of potassium bromide (KBr), strontium sulfate (SrSO_4), and boric acid (H_3BO_3), which together account for only 0.1‰ compared to 30‰ in total salinity.

Figure 4a shows the temperature profiles measured in situ with the thermistor system near the ice surface to a depth of 8.2 cm for every 2-cm interval. The temperature records started at the time of the initial ice growth. The air temperature measured by the meteorological station is also replotted with the dots for reference. From these results, the time constant of the interfacial and subsurface thermal response is about 2.5 hours corresponding to the time lag between the temperature peaks and the maximum solar input (compare Figure 4a and Figure 3a). A closer examination of the temperature extrema indicates a slightly slower response deeper below the air-ice surface. At a depth closer to the ice-water interface, the peak-to-peak variation in temperature in the ice layer became smaller. These observations indicate that the insolation was driving the diurnal thermal cycles.

Since sea ice growth rate depends on the temperature difference between air and water [Adams *et al.*, 1991], diurnal cooling and warming directly influences the ice growth. Figure 4b presents the sea ice growth up to 10 cm in thickness during the 2.5 days of the experiment. The result shows a clear slowdown in the ice growth corresponding to the daytime warming of the ice sheet. In effect, the solar input tends to shut off the growth and consequently halts the salt rejection into the ocean. A comparison of these results and Arctic field observations [Ruffieux *et al.*, 1995; McPherson and Stanton, 1996] shows that the Arctic diurnal thermal responses also have definitive afternoon peak but with broader time width due to longer Arctic insolation hours. In both cases, diurnal thermal cycling effects are pronounced and have similar trends with large diurnal amplitudes.

3.3. Physical Characteristics

At the time of the initial growth, the solar short-wave radiation was high (Figure 3a) and the growth rate was very slow (Figure 4b). This slow growth produced a thin incubation layer with vertical crystallographic c axes and a very low salinity. The formation of the incubation layer had been observed in urea ice in laboratory conditions [Gow, 1984] and in natural sea ice in the Bay of Bothnia [Gow *et al.*, 1992]. This initial layer occupied the top few millimeters (~ 5 mm) as seen in the vertical thin sections in figure 5. Below the incubation layer, ice crystals transitioned to ordinary columnar sea ice with c axes tilted away from nadir and randomly oriented in azimuth. Comparing the top and the bottom horizontal thin sections in Figure 5, we observe the contrast between the granular nature of ice in the incubation layer and the dendritic polycrystalline structure of columnar ice.

A slow growth rate results in more effective brine rejection and consequently less brine entrapment in sea ice [Weeks and Ackley, 1982; Nakawo and Sinha, 1981]. Figure 6 presents salinity profiles of sea ice samples at various growth stages with different thicknesses. The salinity profiles indicate that the near surface layer contained significantly lower salinity in all cases. This is consistent with the formation of the incubation layer at a very low growth rate around solar noon on 19 January. Note that the profiles do not have the usual C shape possibly because of variations in growth rate at different warming and cooling temperatures.

The desalination is apparent in the decrease of bulk salinity as the ice sheet aged and thickened as shown in the top panel of Figure 7. The linear fitting curve has an initial value of 1.20‰ and a negative slope of 0.458‰/cm . The internal salinity loss was primarily

by downward brine flux because the incubation layer hindered the upward brine expulsion and migration. Bulk ice temperatures, obtained by integrating the ice temperature profiles and normalizing over the thickness of the ice sheet, also show the diurnal cycles with high daytime values corresponding to thicknesses of about 0.5 cm, 5 cm, and 10 cm as seen in the middle panel of Figure 7. For each cycle, a quadratic function fits the temperature data and is plotted with the continuous curve.

The bottom panel of Figure 7 shows variations in brine volume versus ice thickness. The data represent calculations from thermodynamic phase equations by Cox and Weeks [1983] based on measured or extrapolated salinity and temperature. The brine volume curve is from fitted salinity and temperature values. A combination of desalination and diurnal effects are both manifest in the brine volume over the 10-cm range of thickness with a general decreasing trend imposing on the thermal cycles. The diurnal cycles in the brine volume are quite significant with a nighttime freeze-up of 50% liquid phase and a daytime recovery of 50% brine volume observed in both cycles.

Brightness temperatures of the ice sheet for both horizontal and vertical polarizations, T_{Bh} and T_{Bv} respectively, at 90 GHz and 50° incident angle show diurnal cycles as seen in Figure 8. The cycles are well defined except for the first few millimeters of the ice growth when the phase transition was inhomogeneous and complicated. Note that the daytime peak at the growth stage between 5 and 6 cm coincides with the ice temperature peak in Figure 7 and with the surface temperature peak replotted as a function of ice thickness in Figure 9. This is because brightness temperatures are sensitive to the physical temperature of the target. Thus, the radiometer observations affirm the diurnal response of the ice sheet. We will use the sea ice physical characteristics under thermal cycling effects

presented above to calculate and to explain the observed diurnal backscatter signature.

4. Backscatter Signatures

4.1 Experimental Observations

The diurnal cycling signature is evident in the C-band backscatter shown in Figure 9 for horizontal polarization. For reference, we present backscatter data together with measurements of sea ice surface temperature. Surface temperature data acquired by the digital thermometer were at the surface area near the scatterometer gantry and thermistor data were at the other end of the GRF pond. The temperatures were relatively homogeneous over the entire ice surface considering measurement uncertainties. Backscatter data for both 25° and 30° incident angles clearly exhibit these characteristics: (a) backscatter diurnal cycles are substantial with variations up to 6 dB, (b) backscatter and temperature cycles are synchronous and well correlated, and (c) backscatter cycles are repeatable along with diurnal thermal variations. Backscatter at other incident angles and polarizations has a similar diurnal signature as shown later in Figure 13 in Section 4.4 for comparisons between theoretical results and experimental data.

Surface salinity measurements do not support the occurrence of any event of brine expulsion to the sea ice surface. This agrees with the existence of the incubation layer, which served as a barrier preventing internal brine from surfacing. Thus, the 6-dB change cannot be related to the surface brine expulsion. As observed in Figure 9, the backscatter peaked at the growth stage of 5.4 cm close to the daytime ice temperature maximum. Figure 9, however, indicates that the backscatter became less correlated with temperature

when the ice sheet grew thicker though the diurnal signature was still prevailing. Toward the end of this experiment, more frost flowers appeared on the ice surface especially in the area corresponding to larger incident angles. The repeatability of backscatter cycles suggests that the scattering mechanism relates to a reversible process, which is responsive to the diurnal thermal cycling. In the following sections, we will take into account these experimental observations in relating the back scatter to physical characteristics of sea ice to explain the diurnal cycles in the scatterometer measurements.

4.2 Sea Ice Electromagnetics

This section discusses the relationship between sea ice electromagnetic characteristics and physical ice properties undergoing diurnal warming and cooling cycles. First, electromagnetic wave propagation, attenuation, reflection, and transmission depend on relative permittivities of the constituents in the inhomogeneous sea ice medium. For the ice background in the sea ice sheet, both real part [Vant *et al.*, 1978] and imaginary part [Tiuri *et al.*, 1984] of the permittivity depend on ice temperature. The permittivity of brine inclusions in the sea ice sheet is also a function of temperature especially for the real part [Stogryn and Desargant, 1983]. Thus, diurnal thermal cycles cause corresponding cycles in the effective permittivity of sea ice, which is a mixture of the background ice and brine inclusions.

Scattering from inhomogeneities such as brine inclusions explicitly relates to brine volume [Nghiem *et al.*, 1993; 1995a-c]. As shown in Figure 7, the fractional volume of brine inclusions follows the diurnal cycles with a slightly decreasing trend due to desalination. Thereby, the cycles in brine volume contribute to corresponding diurnal cycling effects on

backscatter. Moreover, warming and cooling of the sea ice sheet give rise to enlargement and shrinkage of brine pockets [Perovich and Gow, 1991], respectively by melting and freezing of brine pocket walls to keep the phase distribution on the eutectic curve. For millimetric and submillimetric brine scatterers that are much smaller than the wavelength of 60 mm at 5 GHz, the backscattering cross section in the Rayleigh regime varies with the sixth power of the scatterer size [Kong, 1986]. Consequently, backscatter is higher for larger brine pockets at warmer temperatures. However, effects on backscatter caused by thermal diurnal cycling in permittivity, brine volume, and scatterer are competitive. While increases in brine volume and pocket size at a higher temperature lead to backscatter increase, effective permittivity also increases [Nghiem *et al.*, 1996a] and so do attenuation and reflectivity, which decrease the backscatter from the inhomogeneous sea ice layer.

The roughness on the air-ice interface also affects the backscatter diurnal cycles especially at small incident angles. For a given roughness, a higher permittivity in the surface layer increases the surface scattering from sea ice [Nghiem *et al.*, 1996a] with a weak temperature dependence. In fact, we observed some small scale roughness on the surface of the ice sheet during the ice growth. There was no significant change in the roughness as the ice aged because the surface was frozen solid without wind and wave actions. The appearance of some more frost flowers toward the end of the experiment could increase the roughness. However, this effect is not significant otherwise there should be a general increasing trend in the backscatter, which is not supported by the backscatter measurements. For the highly saline thin ice under consideration, the scattering contribution at C band from the lower interface between ice and water is not important as proved experimentally [Nghiem *et al.*, 1996b].

4.3 Diurnal Backscatter Model

The above electromagnetic characteristics of sea ice related to the physical properties undergoing diurnal thermal cycles are necessary in the development of a sea ice scattering model to explain the observation of diurnal backscatter variations. The model needs to account for the contributive and competitive effects of the scattering mechanisms as discussed in the last section. We have developed sea ice models including scattering from inhomogeneities in the ice layer, composite roughnesses on medium interfaces, multiple wave interactions with layer boundaries, and wave propagation and attenuation in complex heterogeneous media [Nghiem *et al.*, 1993; 1995a-c; 1996a]. These models encompass physical, structural, thermodynamic, and electrodynamic properties of sea ice. In this section, we review the theory and present the application for a diurnal backscatter model of sea ice.

Figure 10 represents the scattering configuration of the layered sea ice model. The upper half space is air with permittivity ϵ_0 . The sea ice layer contains ice with random brine inclusions and has a rough surface at the air-ice interface and brine inclusions in the ice layer. The bottom boundary between ice and water has little contribution in the backscatter and is modeled as a planar interface. The lower half space is seawater with permittivity ϵ_2 given by Klein and Swift [1977]. The notations in this model for the media are subscript 0 for air, 1 for sea ice, and 2 for seawater.

For a targeted area A at a distance r from the scatterometer, polarimetric backscattering coefficient $\sigma_{\mu\tau\nu\kappa}$ is

$$\sigma_{\mu\tau\nu\kappa} = \lim_{\substack{r \rightarrow \infty \\ A \rightarrow \infty}} \frac{4\pi r^2}{A} \frac{\langle E_{\mu s} E_{\nu s}^* \rangle}{E_{\tau i} E_{\kappa i}^*} \quad (1)$$

where E is an electric field with its complex conjugate represented with an asterisk, the angular brackets denote the ensemble average, subscripts μ, ν, τ , and κ are h for horizontal or v for vertical polarization, and i and s for incident and scattered fields, respectively.

For scatterers such as brine inclusions in the sea ice sheet, the ensemble average in (1) is determined by

$$\begin{aligned} \langle E_s(\bar{r}) \cdot E_s^*(\bar{r}) \rangle = & \sum_{i,j,k,l,m}^{x,y,z} k_0^4 \int_0^\pi d\psi_{1f} \int_0^{2\pi} d\phi_{1f} p_1(\psi_{1f}, \phi_{1f}) \\ & \int_{V_1} d\bar{r}_1 \int_{V_1} d\bar{r}_1^o C_{1\xi jklm}(\bar{r}_1, \bar{r}_1^o; \psi_{1f}, \phi_{1f}) \\ & [\langle G_{01ij}(\bar{r}, \bar{r}_1) \rangle \langle E_{1k}(\bar{r}_1) \rangle] \\ & [\langle G_{01il}(\bar{r}, \bar{r}_1^o) \rangle \langle E_{1m}(\bar{r}_1^o) \rangle]^* \end{aligned} \quad (2)$$

where k_0 is the free-space wave number, p_1 is the scatterer orientation distribution with Eulerian angles ψ_{1f} and ϕ_{1f} , position \bar{r}_1 or \bar{r}_1^o is in volume V_1 of the sea ice sheet, $\langle G \rangle$ is for the mean dyadic Green's function, and $\langle E \rangle$ is the mean incident field. As seen in the vertical thin section in Figure 5 and other ice samples, the ice crystals are tilted with no preferential azimuthal direction. Thus, we describe the orientation distribution with $p_1 = \sin \psi_{1f} / (4\pi)$ for random orientation

In (I), correlation function $C_{1\xi jklm}$ of the scatterer is [Nghiem *et al.*, 1995a]

$$\begin{aligned} C_{1\xi jklm}(\bar{r}_1, \bar{r}_1^o; \psi_{1f}, \phi_{1f}) = & \langle \xi_{1jk}(\bar{r}_1) \xi_{1lm}^*(\bar{r}_1^o) \psi_{1f}(\bar{r}_1), \phi_{1f}(\bar{r}_1) \rangle \\ = & \int_{-\infty}^{\infty} d\bar{\beta} \Gamma_{1jklm} \Phi_{1\xi}(\bar{\beta}) e^{-i\bar{\beta} \cdot (\bar{r}_1 - \bar{r}_1^o)} \end{aligned} \quad (3)$$

where $\Phi_{1\xi}$ is the normalized correlation function defined in the local coordinates (x', y', z') as [Nghiem *et al.*, 1993]

$$\Phi_\xi(\bar{k}') = \frac{\ell_{x'} \ell_{y'} \ell_{z'}}{\pi^2 (1 + k_{x'}'^2 \ell_{x'}^2 + k_{y'}'^2 \ell_{y'}^2 + k_{z'}'^2 \ell_{z'}^2)^2} \quad (4)$$

in which $\ell_{x'}$, $\ell_{y'}$, and $\ell_{z'}$ are three different correlation lengths for an ellipsoidal scatterer in the local coordinates (x', y', z') related to (x, y, z) by Eulerian angles ψ_{1f} and ϕ_{1f} . The variance Γ_{1jklm} of permittivity fluctuations in the correlation function relates to the brine volume fraction in the sea ice sheet. The dependence of the brine volume on diurnal cycles governed by the thermodynamic phase equilibrium thereby contributes to the backscatter diurnal variations.

While giving rise to the backscattering, brine inclusions also influence electromagnetic wave propagation and attenuation characterized with effective permittivity ϵ_{1eff} . For sea ice with randomly oriented brine pockets, the effective permittivity is isotropic and expressed as

$$\epsilon_{1eff} = \epsilon_{1g} + \epsilon_0 \left[1 - \xi_{1eff} \langle S_1 \rangle \right]^{-1} \xi_{1eff} \quad (5)$$

where $\langle S_1 \rangle$ is the average of the polarizability of ellipsoidal brine inclusions [Nghiem *et al.*, 1995a]. The term $\bar{\epsilon}_{1g}$ in (5) represents the quasi-static effect, which has the form of Polder-van Santen mixing formula and relates to permittivities of the constituents in sea ice. Thus, diurnal thermal effects on permittivities of the ice background and brine inclusions are present even in the zeroth-order dielectric mixing. Effective scatterer ξ_{1eff} accounts for scattering effects on wave propagation and attenuation. The same form of correlation function shown above also characterizes ξ_{1eff} ; therefore, it directly varies with the diurnal cycles in brine volume and scatterer size. This includes into the model the competitive effect in scattering mechanisms as discussed in Section 4.2.

For rough surface scattering in layered media, we have developed and presented the model [Nghiem *et al.*, 1995b]. The surface scattering is a function of wave vector; thus, this mechanism is less sensitive to the diurnal effect since the wave number depends only on

the complex square root of the diurnally cycled permittivity. We have presented complete and explicit mathematical expressions for the composite scattering including volume and surface mechanisms and for effective permittivity of sea ice elsewhere [Nghiem *et al.*, 1993; 1995a-c; 1996a].

4.4 Data Comparisons

The model requires permittivities of ice background and brine inclusions in the inhomogeneous sea ice sheet. Empirical functions of these permittivities depending on temperature are available in given references as discussed in Section 4.2. With measured temperatures, these functions determine variations in the model input permittivities under effects of diurnal thermal cycles. Another important input is the brine volume, which clearly shows the warming and cooling effects as seen in the bottom panel in Figure 7. For the rough surface, we use a height standard deviation of 0.65 mm and a correlation length of 2.5 cm to model the frozen solid ice surface for all growth stages. In this case, variations in the effective permittivity of sea ice contribute to the diurnal signature in the surface scattering.

For brine inclusions, the correlation lengths are $\ell_{1y'} = 0.05$ mm and $\ell_{1x'} = \ell_{1z'}/2 = 1$ mm. We obtain these parameters by matching the backscatter data at the growth stage of 3-cm thickness. The change in brine volume at other growth stages then determines the brine size and thus the correlation lengths with the same axial ratios for all cases. With this approach, measured temperature and salinity govern all the model parameters for all growth stages without allowing any extraneous change in these parameters. Restrained under the sea ice thermodynamics and electrodynamics, backscatter calculated from the

model needs to reproduce and to explain the diurnal warming and cooling cycles exhibited in the backscatter signature measured by the scatterometer.

Figure 11 compares calculated and measured polarimetric backscatter as a function of incident angles from 20° to 55° for the intermediate growth stage corresponding to 5.4-cm thick ice. In general, backscattering coefficients σ_{hh} and σ_{vv} compare well. However, theoretical cross-polarized backscatter σ_{hv} is lower than experimental data. This is because more complicated structures in sea ice and higher order scattering are not considered in the model. For the complex correlation coefficient ρ , the model magnitude is slightly higher than experimental data; and both calculated and measured phases are small for most incident angles. At large incident angles such as 50° and 55° , measured magnitudes of ρ are much lower and phases of ρ are higher than the calculated ones. On the ice surface at these incident angles, some frost flowers appeared at this growth stage, which are not included in the model.

Polarization signatures, which are normalized backscatter σ_n at all polarizations including linear, circular, and elliptical waves [Nghiem et al., 1993], are plotted as a function of orientation and ellipticity angles in Figure 12 for the 5.4-cm thick ice at 40° incident angle. The computed and measured polarization signatures have the same shape as observed in Figure 12. Both polarization signatures peak in the middle where orientation angle α_c is 90° and ellipticity angle β_c is indicating that the vertical linear polarization gives a maximum return above all possible polarization states. The pedestal in the calculated signature, however, is lower implying a lower depolarizing effect in the theory as compared to the measured results.

For all stages of the sea ice sheet over the 2 diurnal thermal cycles, Figure 13 shows

comparisons of diurnal backscatter signatures between theory and experiment at incident angles from 25° to 50.0° . At all incident angles have higher backscatter during the warm daytime and lower during nighttime. While absolute backscatter is larger at the small incident angle of 25° , diurnal variations at this angle are smaller compared to variations at larger incident angles. Overall, theoretical backscatter follows the diurnal cycling trends in experimental data. Calculations and data for copolarized backscatter σ_{hh} and σ_{vv} are in good agreement. An exception is the high measured data at 35° - 50.0° corresponding to 7.1-cm thick ice, which could be caused by effects from the side of the GRF pool in this singular case when the antenna was turned too much in azimuth toward the cement edge of the pool. Calculated cross-polarized returns are lower than measured data which have large fluctuations and the diurnal cycles are not well defined. In general, the model based on physical properties of sea ice undergoing diurnal warming and cooling cycles captures the diurnal cycling effects as observed in the measurements.

5 . Summary

We successfully carried out an experiment at the Geophysical Research Facility in the Cold Regions Research and Engineering Laboratory to study the signature of diurnal thermal cycling in backscatter from thin sea ice. The ice sheet grew from open water with a salt mixture similar to sea water to a thickness of 10 cm in 2.5 days extending over 2 diurnal cycles. During the ice growth, we took polarimetric backscatter with the Jet Propulsion Laboratory polarimetric scatterometer at C band, together with sea ice characterization and environmental parameters.

During this experiment in the winter of 1994, the temperature was similar to the cold Arctic winter condition with the low down to -36°C during nighttime and the daytime high at only -12°C . The amplitude of midlatitude winter solar radiation was close to the Arctic condition. Together with a calm atmosphere, these conditions were particularly suitable for the study of diurnal signature in backscatter. Correlated with the insolation cycles, ice temperature, brine volume, growth rate, thickness, and emission showed diurnal cycles with a lag of approximately 2.5 hours from the solar-wave radiation peak at solar noon. The initial growth was about 2 hours before high noon and an incubation layer containing low salinity formed the top layer of the sea ice sheet preventing surface brine expulsion.

Experimental measurements reveal repeatable diurnal cycles in backscatter, which are synchronous and well correlated with the cycles in sea ice physical parameters. The backscatter diurnal variations was substantial with up to 6-dB changes between day and night. We use a diurnal sea ice backscatter model based on thermal and electromagnetic properties of sea ice to calculate backscatter and to explain the diurnal cycling trend in experimental observations. The composite model including both volume and surface interactions accounts for contributive as well as competitive effects in the scattering mechanisms due to diurnal variations in physical parameters of sea ice. Calculations for copolarized backscatter compare well with data. Theoretical cross-polarized backscatter is lower than measurements because the theory does not include complicated ice conditions such as frost flowers and ignores higher order scattering. Since this work is for backscatter at C-band and all polarizations, it is useful for application to spaceborne radars such as ERSs, ERS-2, ERSAT, and RADARSATs. The important implication of the results in this paper is that

the substantial diurnal variations in backscatter are imperative for inversion algorithms to retrieve sea ice geophysical parameters from satellite SAR and scatterometer data. This is particularly relevant to sun synchronous satellites which acquires data along ascending and descending orbit paths at different times of the day.

Acknowledgments. The research described in this paper was performed by the Center for Space Microelectronics Technology, Jet Propulsion Laboratory, California Institute of Technology, and was sponsored by the office of Naval Research (ONR), through an agreement with the National Aeronautics and Space Administration. The research by the U. S. Army CRREL was under ONR contracts N00014-95-MP-3002 and N00014-95-MP-3019, by the Massachusetts Institute of Technology under ONR contracts N00014-89-J-1107 and N00014-92-J-4098, and by the University of Washington under ONR contracts N00014-89-J-1140 and N00014-89-J-3132.

References

- Adams, C. M., Jr., D. N. French, and W. D. Kingery, Solidification of sea ice, *J. Glaciol.*, **3**, 745-760, 1960.
- Barber, D. G., E. F. LeDrew, D. G. Flett, M. Shokr, and J. Falkingham, Seasonal and diurnal variations in SAR signatures of landfast sea ice, *IEEE Trans. Geosci. Remote Sens.*, **30**(3), 638-642, 1992.
- Barber, D. G., T. N. Papakyriakou, and E. F. LeDrew, On the relationship between energy fluxes, dielectric properties, and microwave scattering over snow covered first-year sea ice during the spring transition period, *J. Geophys. Res.*, **99**(C11), 22401-22411, 1994.
- Cox, G. F. N., and W. F. Weeks, Equations for determining the gas and brine volumes in sea-ice samples, *J. Glaciol.*, **29**(12), 306-316, 1983.
- Gow, A. J., and W. F. Weeks, The internal structure of fast ice near Narwhal Island, Beaufort Sea, Alaska, *Rep. 77-29*, U. S. Army Corps of Engineers, Cold Regions Research and Engineering Laboratory, Hanover, N. H., 1977.
- Gow, A. J., Crystalline structure of urea ice sheets used in modeling experiments in the CRRRL test basin, *Rep. 84-24*, U. S. Army Corps of Engineers, Cold Regions Research and Engineering Laboratory, Hanover, N. H., 1984.
- Gow, A. J., S. A. Arcone, and S. G. H. Grew, Microwave and structural properties of saline ice, *Rep. 87-20*, U. S. Army Corps of Engineers, Cold Regions Research and Engineering Laboratory, Hanover, N. H., 1987.
- Gow, A. J., D. A. Meese, D. K. Perovich, and W. B. Tucker III, The anatomy of a freezing

- 101(1), *J. Geophys. Res.*, 95(C10), 18221-18232, 1990.
- Gow, A. J., W. F. Weeks, F. Kosloff, and S. Carsey, Petrographic and salinity characteristics of brackish water ice in the Bay of Bothnia, *Rep. 92-13*, U. S. Army Corps of Engineers, Cold Regions Research and Engineering Laboratory, Hanover, N. H., 1992.
- Grenfell, T. G., and A. W. Lohanick, Temporal variations of the microwave signatures of sea ice during the late spring and early summer near Mould Bay NWT, *J. Geophys. Res.*, 90(C3), 5063-5074, 1985.
- Ikeda, M., Snow cover detected by diurnal warming of sea ice/snow surface off Labrador in NOAA imagery, *IEEE Trans. Geosci. Remote Sens.*, 27(5), 552-560, 1989.
- Klein, L. A., and C. Swift, An improved model for the dielectric constant of sea water at microwave frequencies, *IEEE Trans. Antennas Propagat.*, AP-25(1), 104-111, 1977.
- Kong, J. A., *Electromagnetic Wave Theory*, John Wiley, New York, 1986.
- LeadEx Group, The LeadEx Experiment, *EOS Trans. AGU*, 74, 35, 393, 1993.
- McPhee, M. G., and T. P. Stanton, Turbulence in the statically unstable oceanic boundary layer under Arctic leads, *J. Geophys. Res.*, 101(C3), (3409-6428, 1996.
- Neumann, G., and W. J. Pierson, Jr., *Principles of Physical Oceanography*, Prentice-Hall, Inc., Englewood Cliffs, N. J., 1966.
- Nghiem, S. V., R. Kwok, J. A. Kong, and R. J. Shin, A model with ellipsoidal scatterers for polarimetric remote sensing of anisotropic layered media, *Radio Sci.*, 28(5), (j87-703, 1993.
- Nghiem, S. V., C-band polarimetric scatterometer: System, operation, sensitivity and calibration, *Sea Ice Electromagnetics Workshop*, Hanover, New Hampshire, September 14-16, 1993.

- Nghiem, S. V., R. Kwok, S. H. Yuch, J. A. Kong, M. A. Tassoudji, C. C. Hsu, and R. T. Shin, Polarimetric scattering from layered media with multiple species of scatterers, *Radio Sci.*, , 30(4), **835-W?**, 1995a.
- Nghiem, S. V., R. Kwok, S. H. Yuch, and M. R. Drinkwater, Polarimetric signatures of sea ice, 1, Theoretical model, *J. Geophys. Res.*, 100(C7), 13665-13679, 1995b.
- Nghiem, S. V., R. Kwok, S. H. Yuch, and M. R. Drinkwater, Polarimetric signatures of sea ice, 2, Experimental observations, *J. Geophys. Res.*, 100(C7), 13681-13698, 1995c.
- Nghiem, S. V., R. Kwok, J. A. Kong, R. T. Shin, S. A. Arcone, and A. J. Gow, An electrothermodynamic model with distributed properties for effective permittivities of sea ice, *Radio Sci.*, , 31(2), **297-311**, 1996a.
- Nghiem, S. V., R. Kwok, S. H. Yuch, A. J. Gow, D. K. Perovich, C. C. Hsu, K. H. Ding, and J. A. Kong, Evolution in polarimetric signatures of thin saline ice under constant growth, submitted for publication in *Radio Science*, 1996b.
- Perovich, D. K., and A. J. Gow, A statistical description of microstructure of young ice, *J. Geophys. Res.*, 96(C9), 16943-16953, Sept. 1991.
- Ruffieux, D., P. O. G. Persson, C. W. Fairall, and D. E. Wolfe, Ice pack and lead surface energy budgets during LEADDEX 1992, *J. Geophys. Res.*, , 100(C3), 4953-4962, 1995.
- Stogryn, A., and G. J. Desargant, The dielectric properties of ice in sea ice at microwave frequencies, *IEEE Trans. on Antennas and Propagat.*, AP-33(5), **523-532**, May 1985.
- Tiuri, M. E., A. H. Sihvola, E. G. Nyfors, and M. T. Hallikainen, The complex dielectric constant of snow at microwave frequencies, *IEEE Journal of Ocean Engineering*, OE-9(5), **377-382**, December 1984.
- U. S. Army TECOM Hanover Meteorological Team, Monthly meteorological data, CR-

REFL test (d)], *Intern. Rep. 1123*, Atmos. Sci. Div., U.S. Army Corps of Engineers, Cold Regions Research and Engineering Laboratory, Hanover, N. H., 1994.

Vant, M. R., R. O. Ramseier, V. Makios, The complex-dielectric constant of sea ice at frequencies in the range 0.1-40 GHz, *J. Applied Phys.*,, **49**(3), 1264-1280, 1978.

List of Figures

Figure 1 Experimental setup at the Geophysical Research Facility in the Cold Regions Research and Engineering Laboratory. (a) The upper panel is top view and (b) the lower panel is side view. This diagram is not drawn to scale.

Figure 2 Photograph of the JPL C-band scatterometer antenna mounted on the positioner together with the RF box. The whole fixture was bolted 011 the double 1 beams above the GRF pool at CRREL.

Figure 3 Meteorological conditions: (a) the top panel shows short-wave radiation from 0.3 to 3 μm with the continuous curve and long-wave incident radiation from 3 to 50 μm with the dotted curve and (b) the bottom panel is air temperature measured at the meteorological station with the dotted curve and at the GRF pond with the crosses.

Figure 4 Diurnal response in temperature of the sea ice sheet growing under warming and cooling cycles: (a) temperature profiles Of the sea ice and sea water are represented by continuous curves and the dotted curves is air temperature at the meteorological station plotted for reference; and (b) growth in sea ice thickness over 2.5 days with 2 diurnal cycles.

Figure 5 Horizontal and vertical thin sections Of sea ice for several growth stages at thicknesses of (a) 2.3 cm, (b) 4.0 cm, and (c) 8.0 cm. The millimeter bar under the horizontal thin section of the 2.3- cm ice sample represents the scale for all horizontal thin sections. The ruler with millimeter marking on the top

right corner of the 8-cm vertical thin section is the scale for all vertical thin sections. The incubation layer is evident in approximately the top 5 mm of all vertical thin sections.

Figure 6 Salinity profiles for several growth stages at thicknesses of 4, 5, 7, 9, and 11 cm. Near surface ice layer has low salinity in all cases indicating the incubation layer.

Figure 7 Bulk properties of the ice sheet as functions of thickness for all growth stages in 2 diurnal cycles: (a) the top panel is for bulk salinity, (b) the middle panel for average ice temperature, and (c) the bottom panel for fractional brine volume.

Figure 8 Brightness temperatures of the sea ice sheet at 90 GHz and 50° incident angle: (a) the top panel is T_{Bh} for horizontal polarization and (b) the bottom panel is T_{Bv} for vertical polarization. Symbols are measured data and curves are piecewise quadratic fits for each diurnal thermal cycle. The fits exclude data at early growth stages of 4 mm or less when the phase transition was inhomogeneous and complicated.

Figure 9 Observed diurnal cycles in horizontally polarized backscatter for all growth stages with warming and cooling cycles shown in ice surface temperature. For backscatter, the filled circles are at 25° incident angle and plusses are at 300° incident angle. For temperature, the open circles are data taken with a digital thermometer on sea ice surface near the scatterometer area and crosses are data obtained with thermistors on the ice surface at the far end of the GRF

pool.

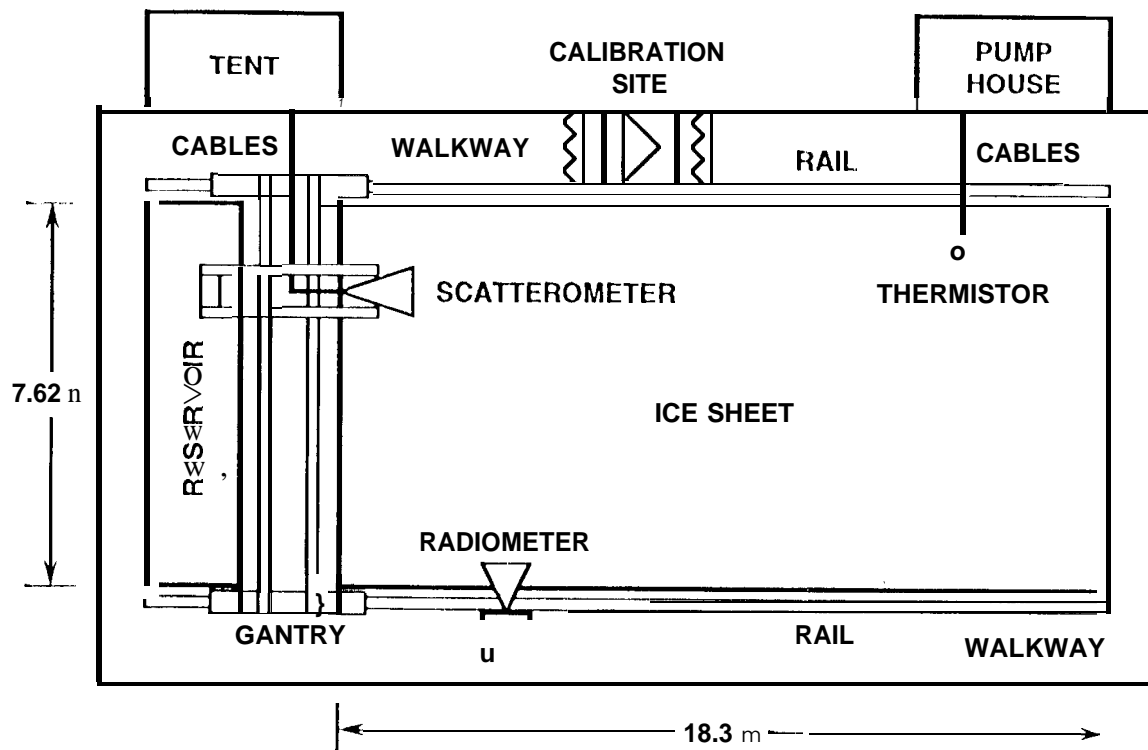
Figure 10 Scattering configuration of the composite inhomogeneous layered model for diurnal backscatter from sea ice.

Figure 11 Comparison of polarimetric backscatter data and model calculations as functions of incident angle for the intermediate growth stage at 5.4-cm thick ice: (a) The top panel is for backscattering coefficients σ_{hh} , σ_{vv} , σ_{hv} , and (b) the middle panel for magnitude of complex correlation coefficient ρ between horizontal and vertical returns, and (c) the bottom panel for phase of ρ .

Figure 12 Comparison of polarization signatures of sea ice versus polarization orientation and ellipticity angles at 400° incident angle for the intermediate growth stage at 5.4-cm thick ice: (a) polarization signature from measured data and (b) polarization signature from model results.

Figure 13 Comparisons Of measured and calculated backscatter for all growth stages in 2 diurnal thermal cycles for incident angles at 25°, 30°, 35°, 40°, 45°, and 50°. For measurements, squares represent σ_{hh} , triangles are σ_{vv} , and crosses are σ_{hv} . For calculations, continuous, dashed, and dash-dotted curves represent σ_{hh} , σ_{vv} , and σ_{hv} , respectively.

(a) Top view



(b) Side view

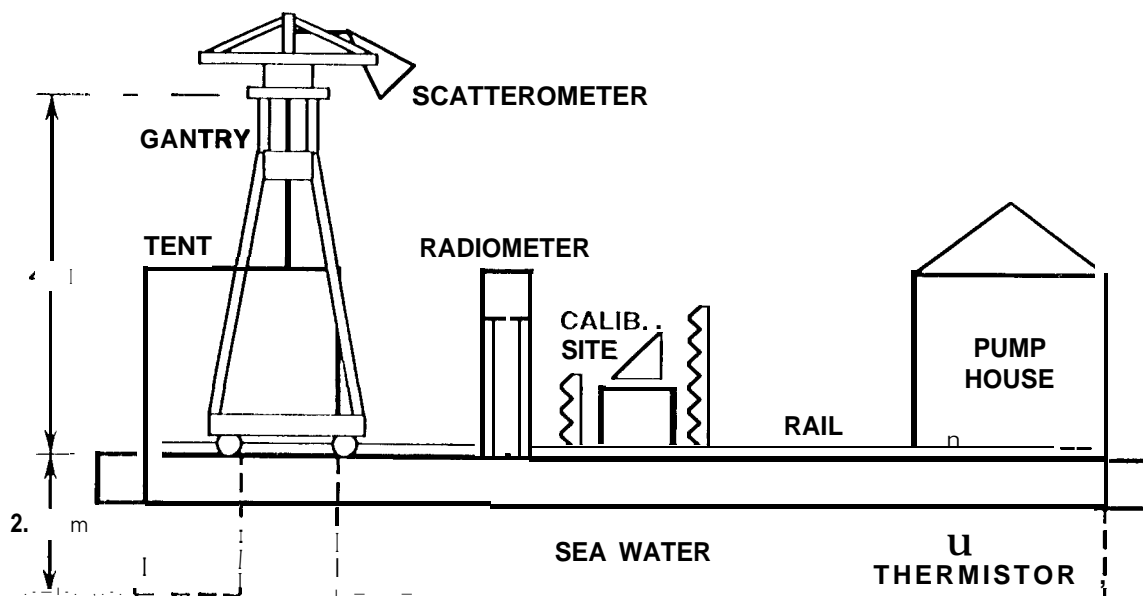


Figure 1

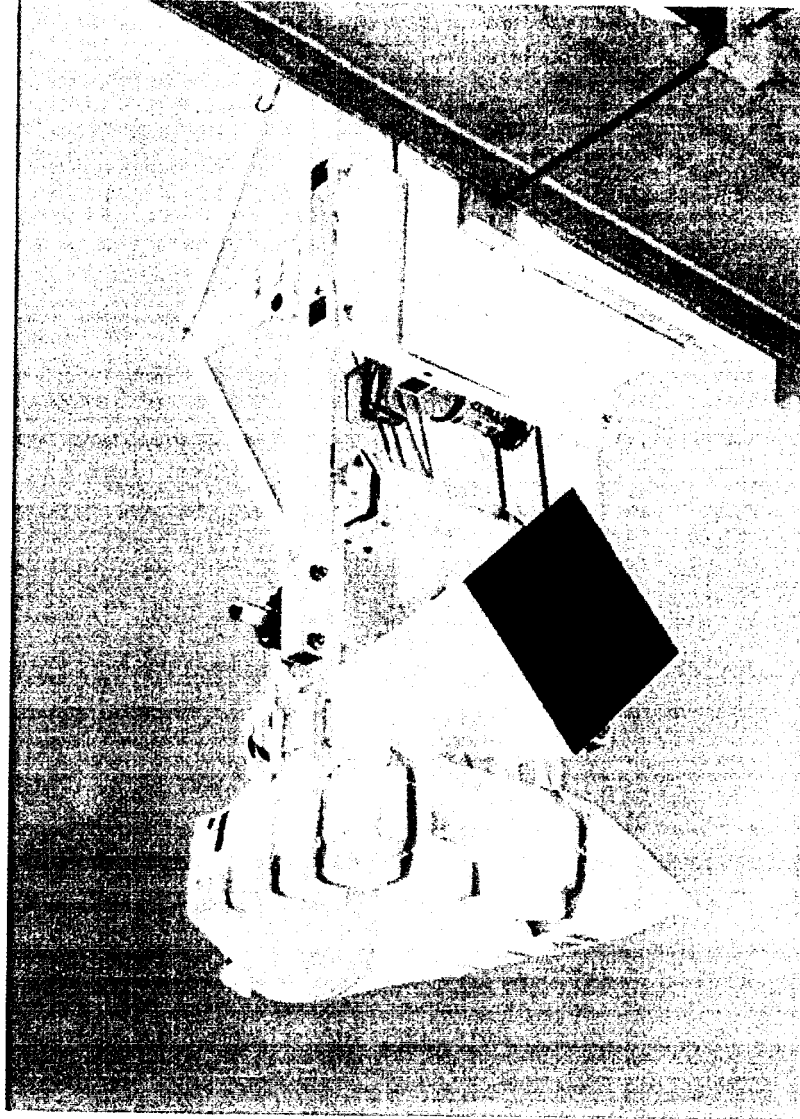
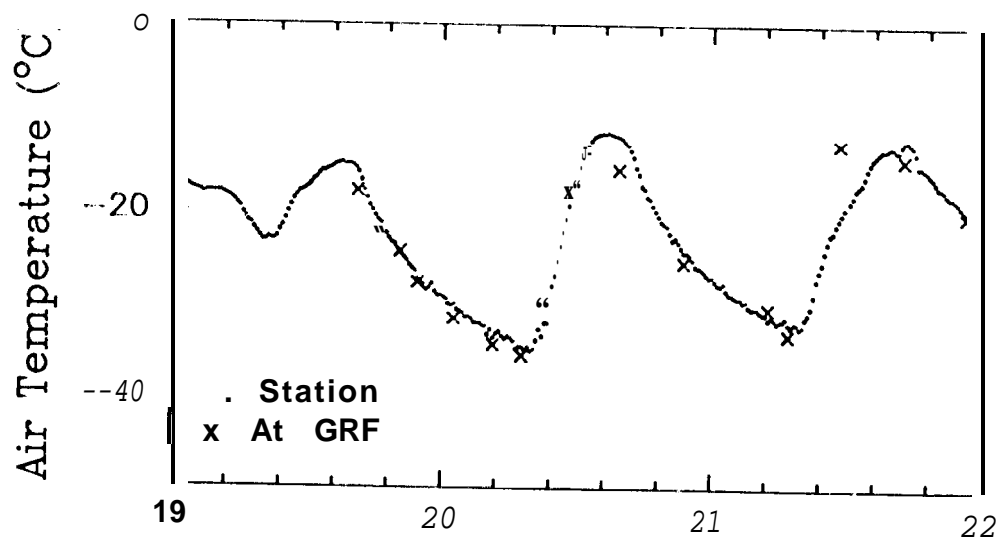
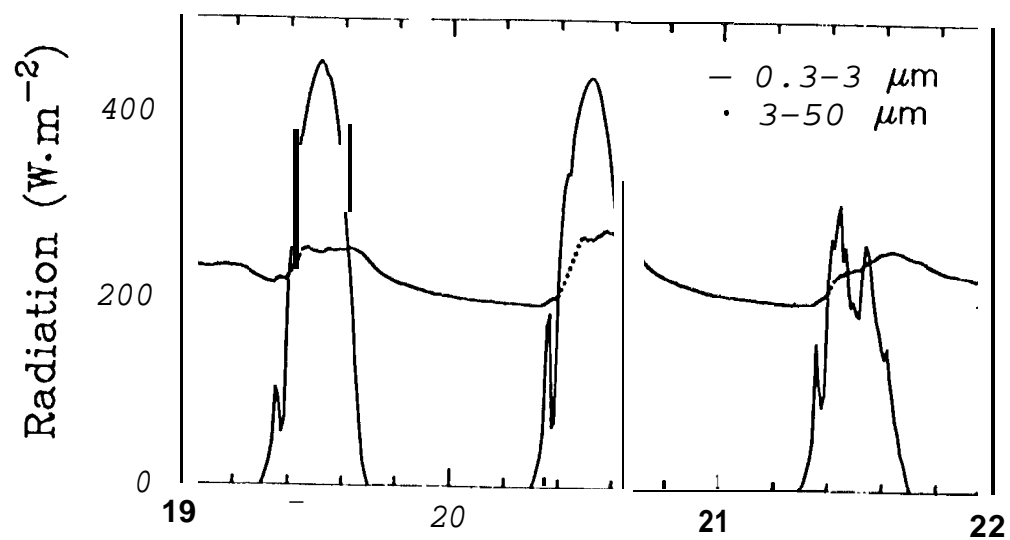


FIGURE 2



Local Julian Day

FIGURE 3

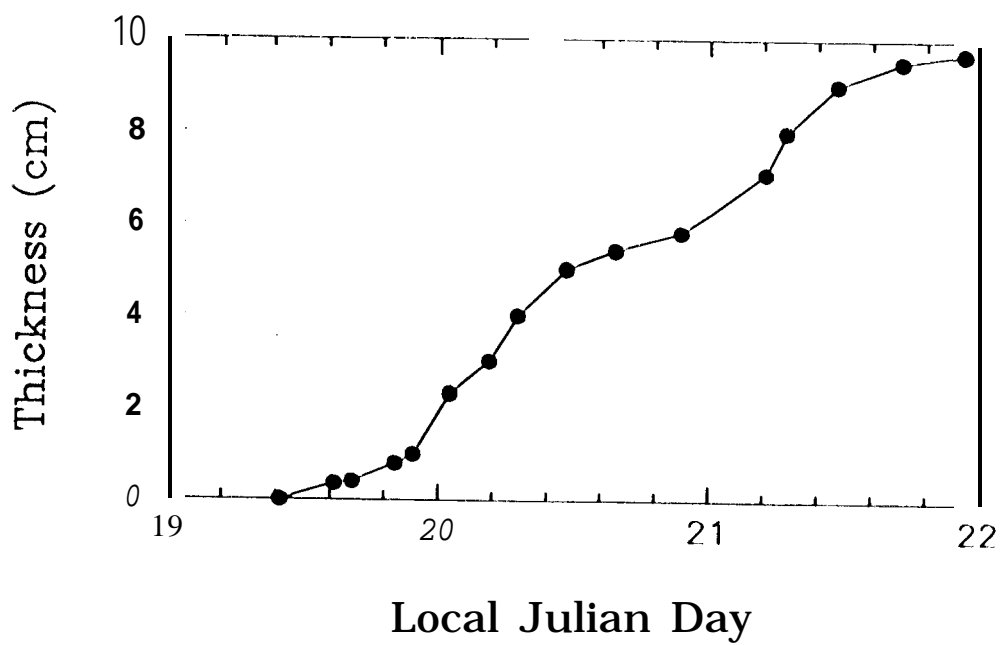
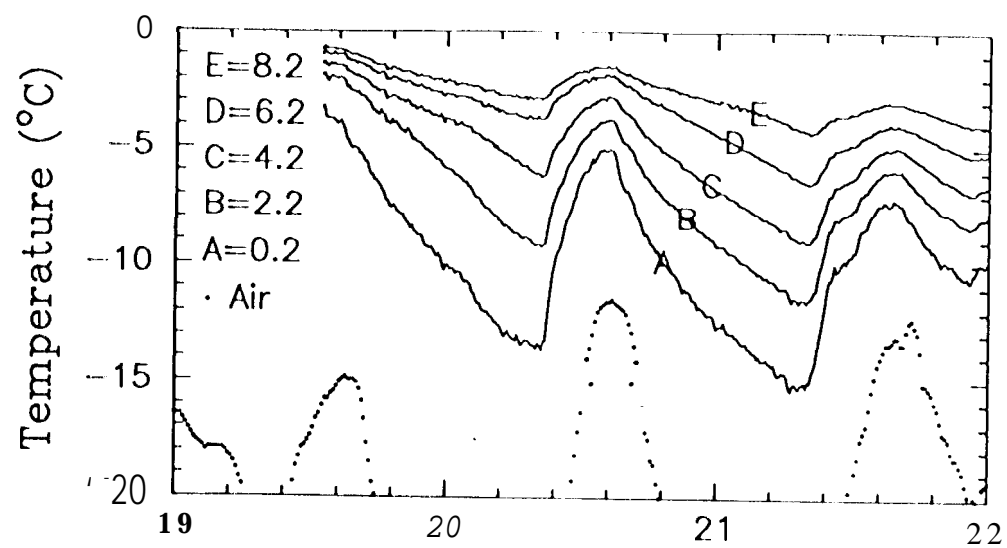
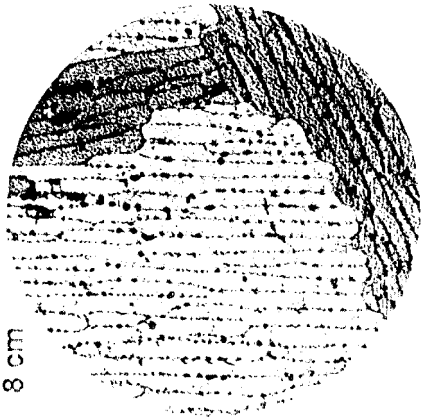
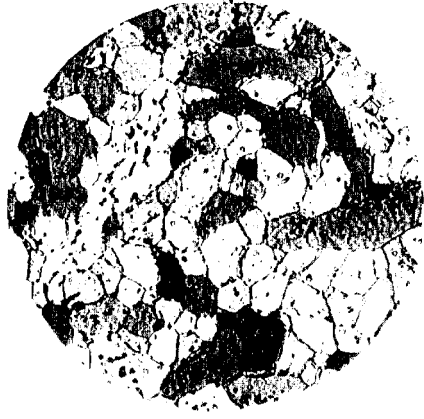
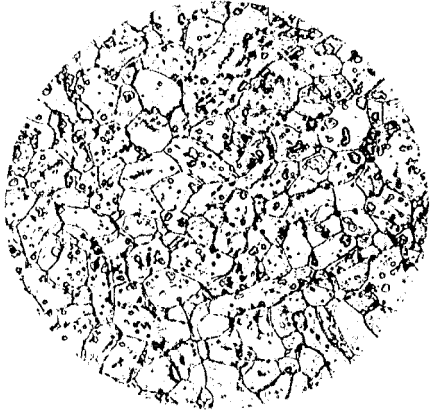


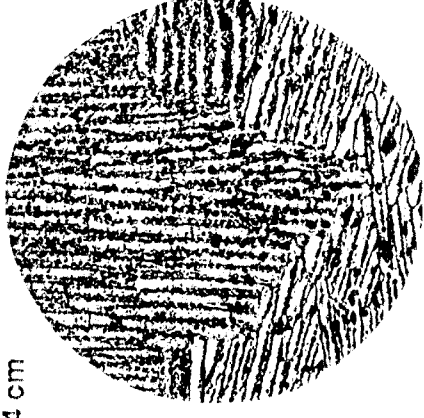
FIGURE 4



8 cm



4 cm



2.3 cm

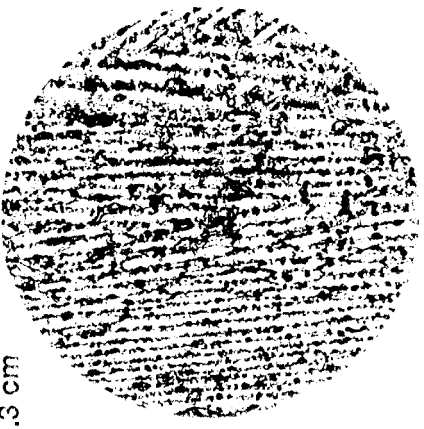


FIGURE 5

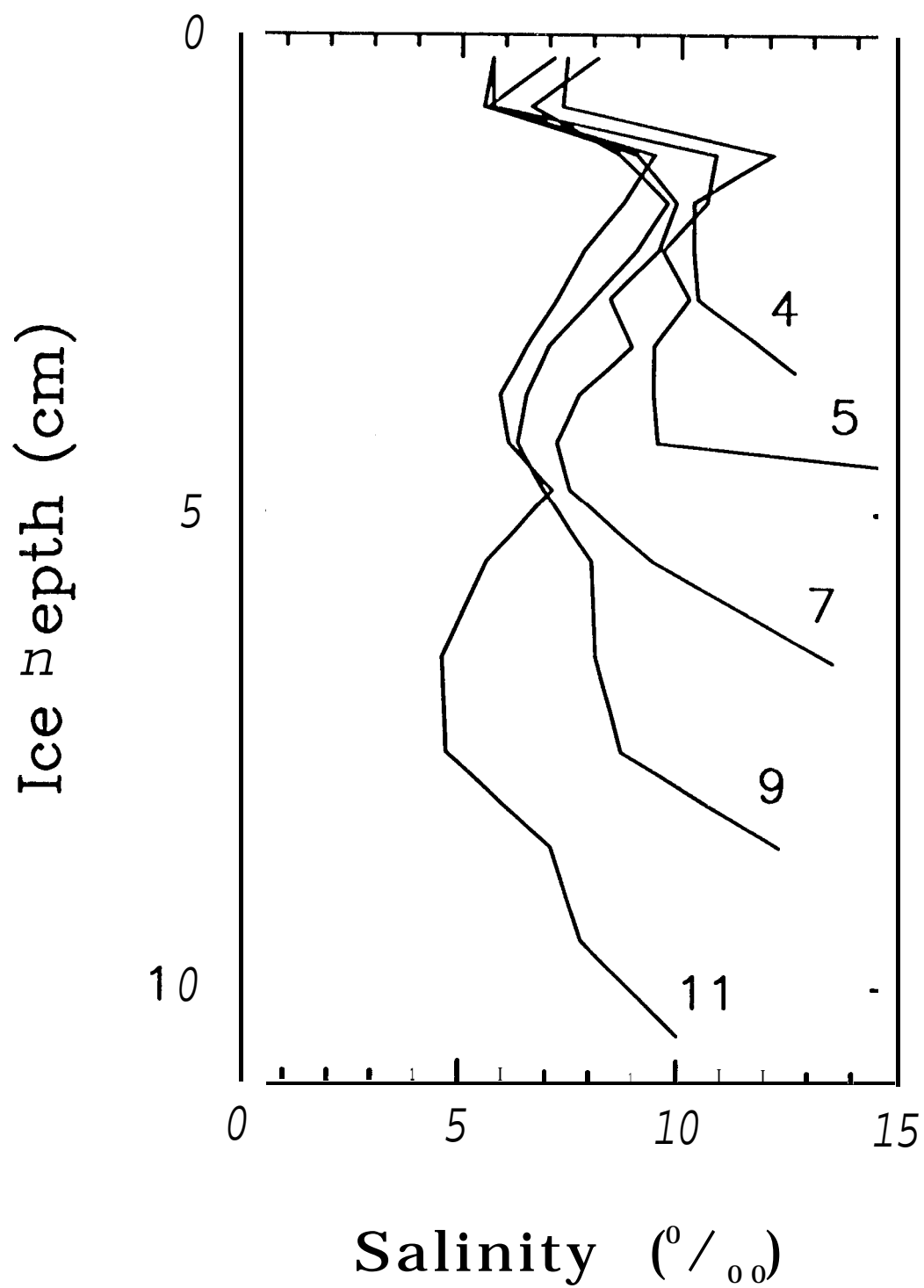


FIGURE 6

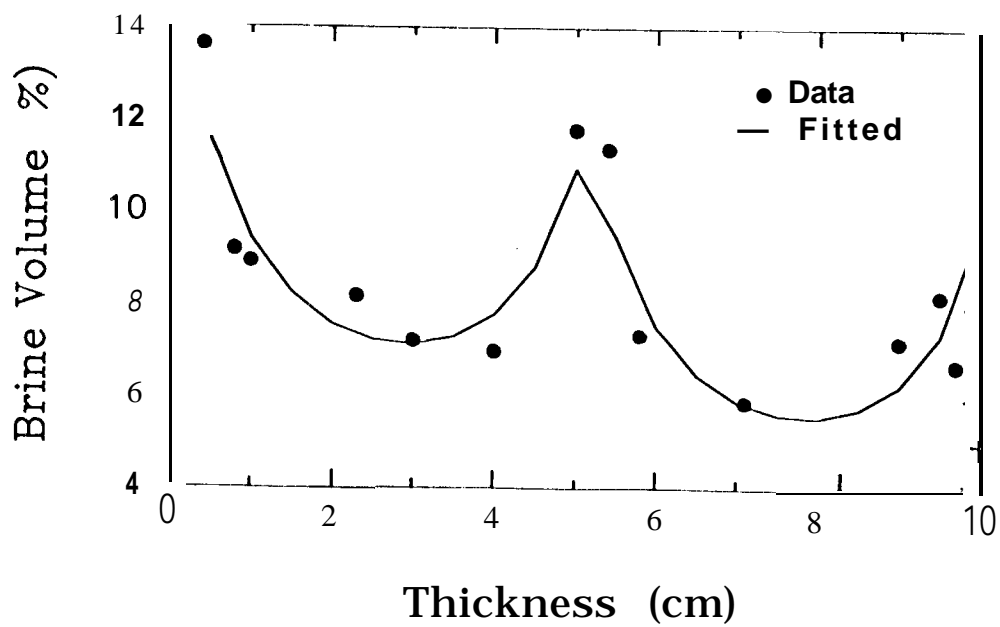
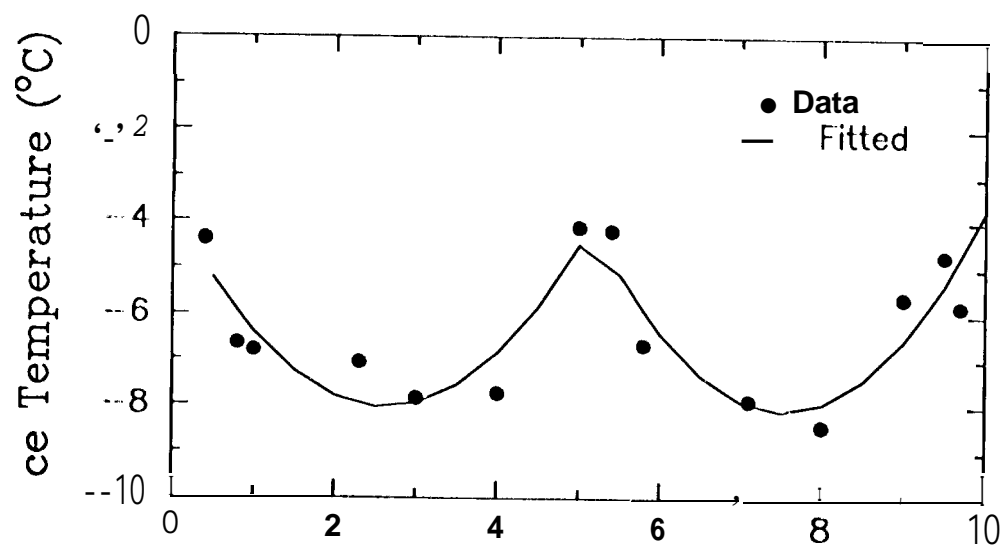
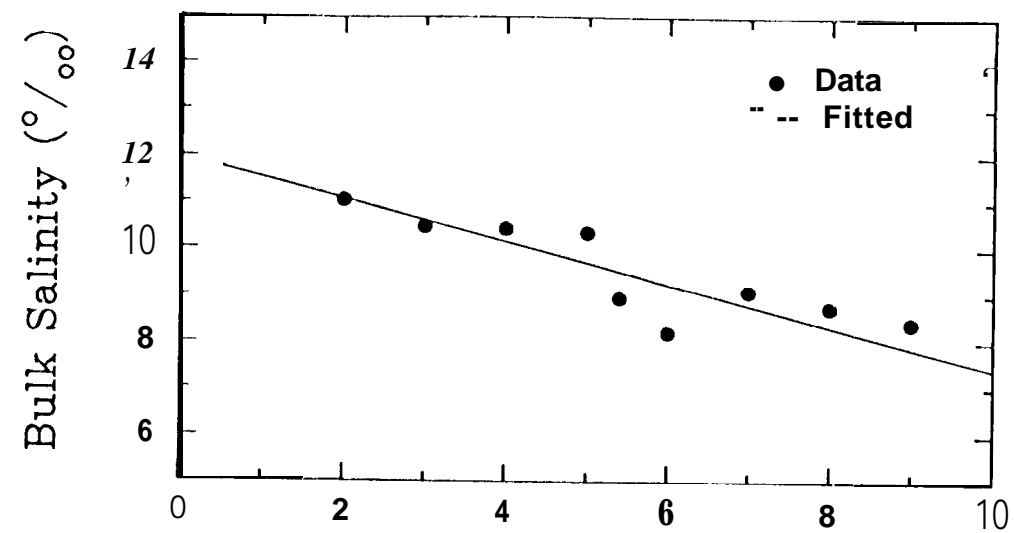


FIGURE 7

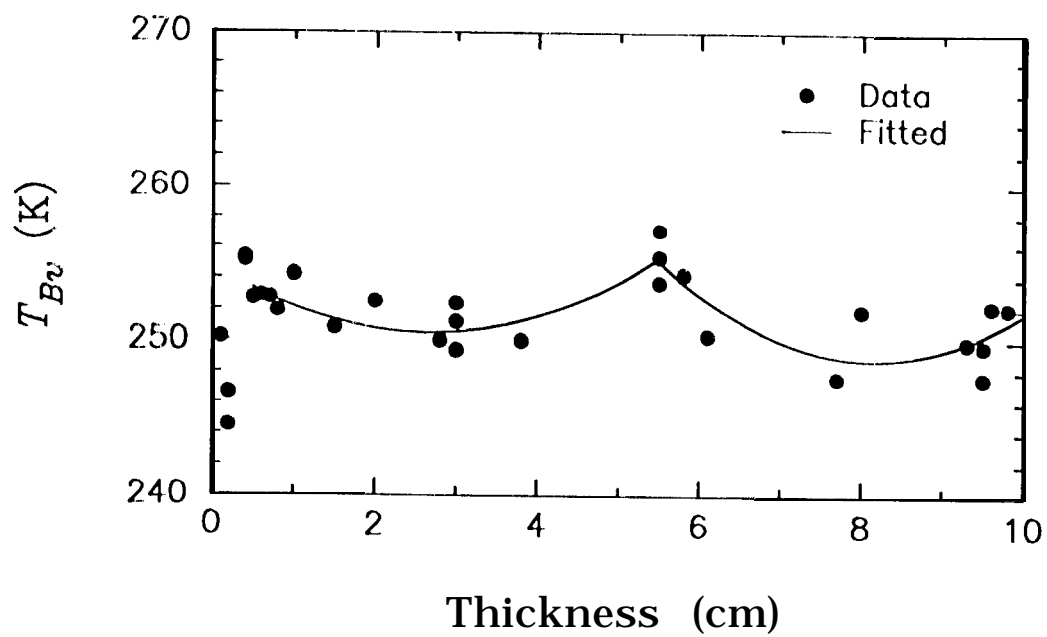
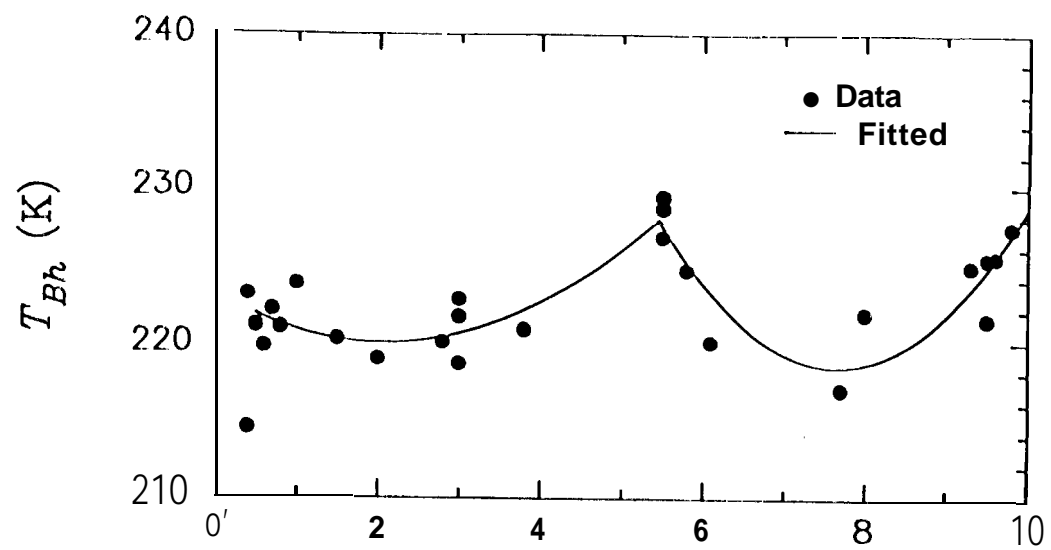


FIGURE 8

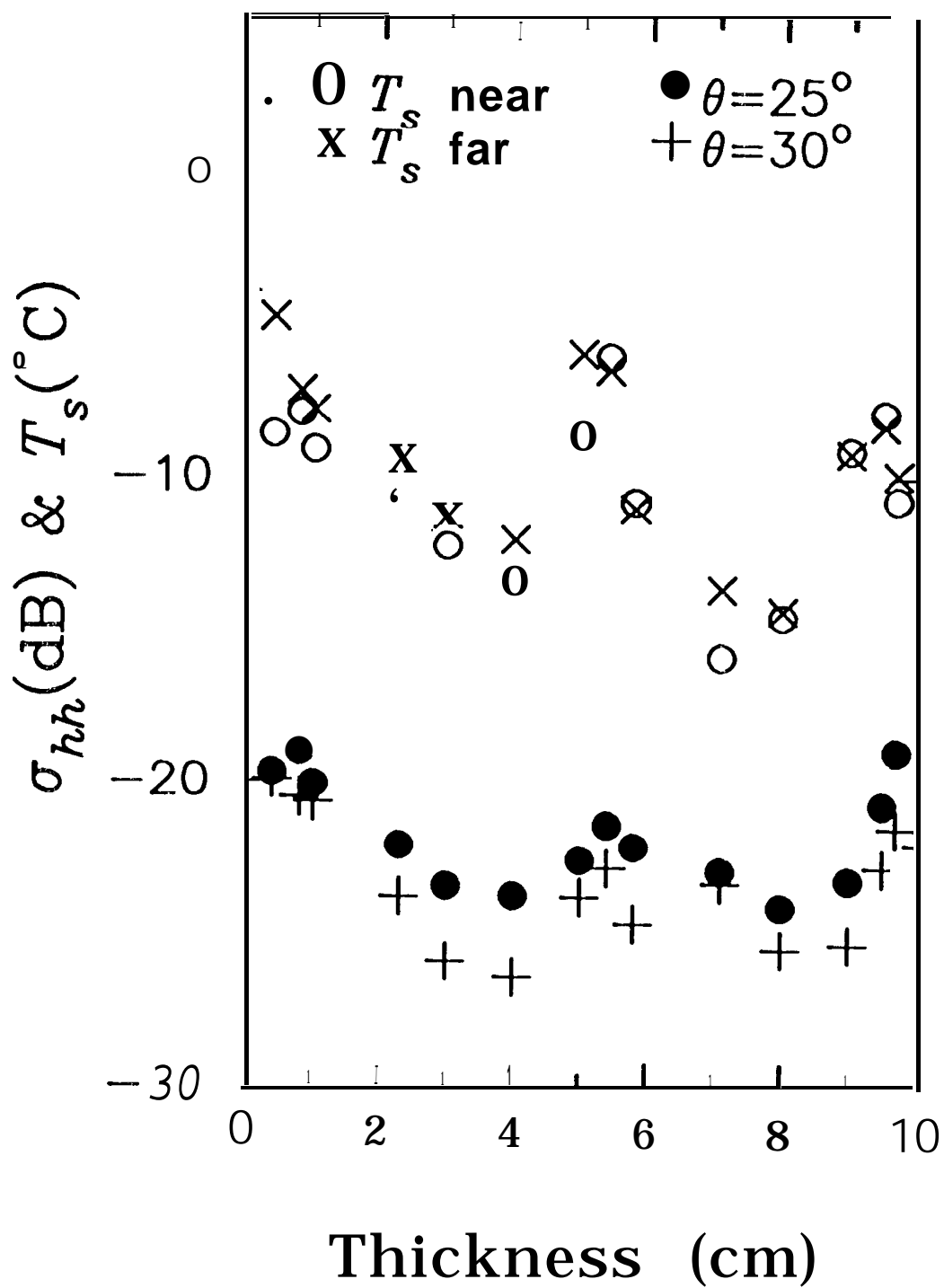


FIGURE 9

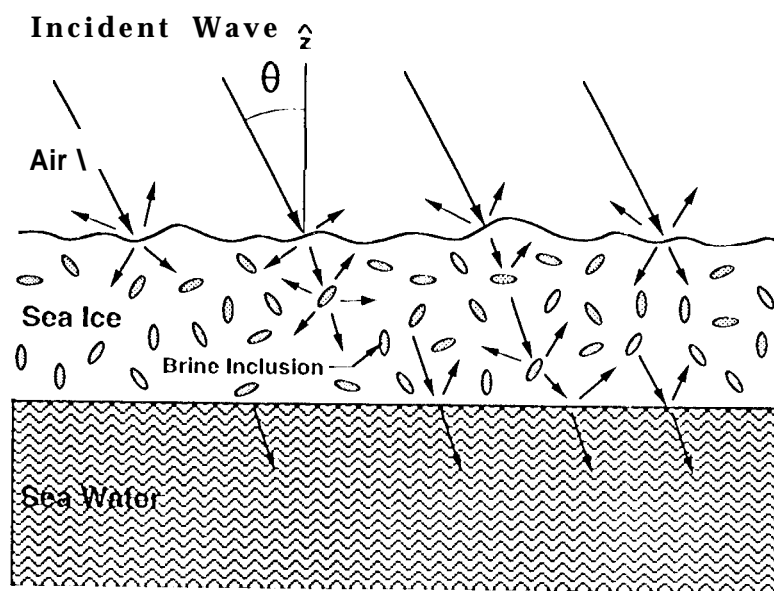


FIGURE 10

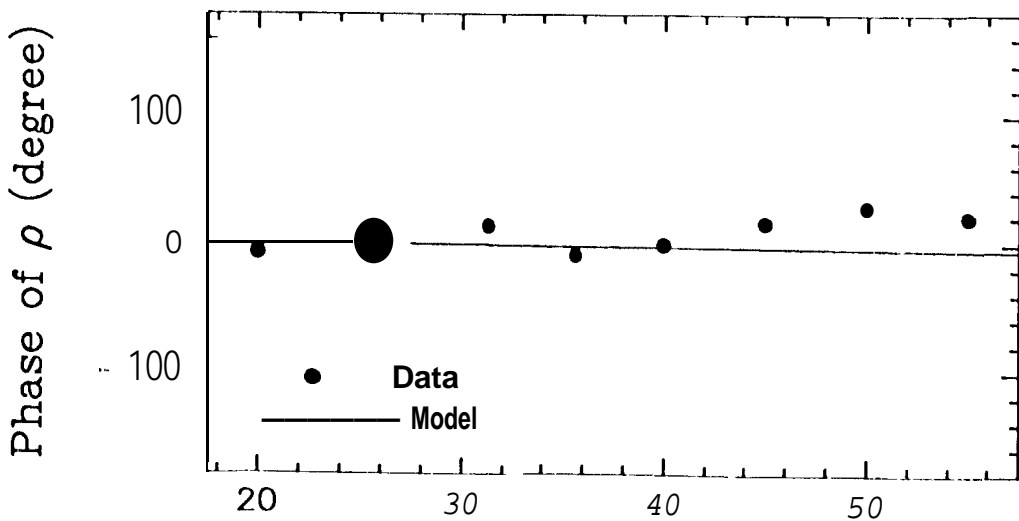
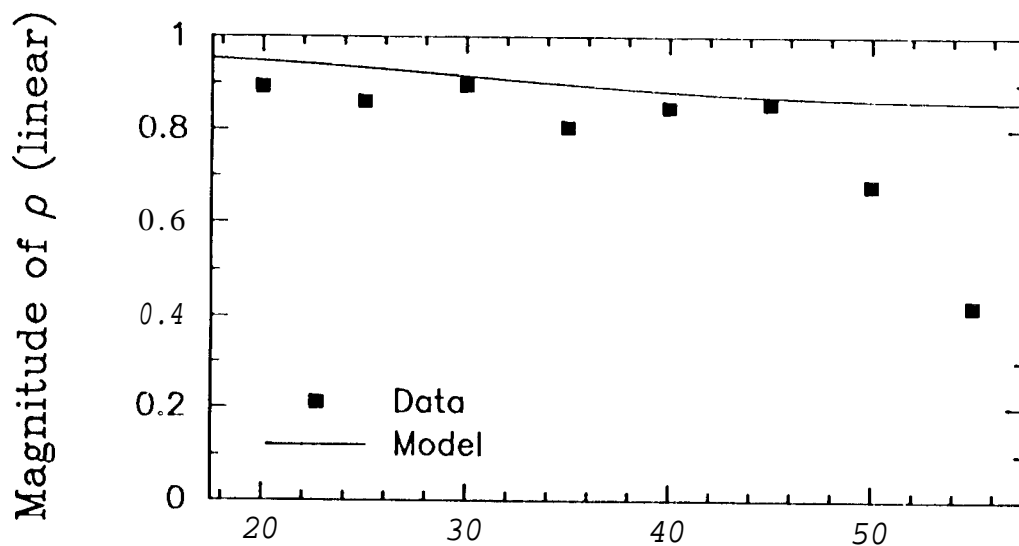
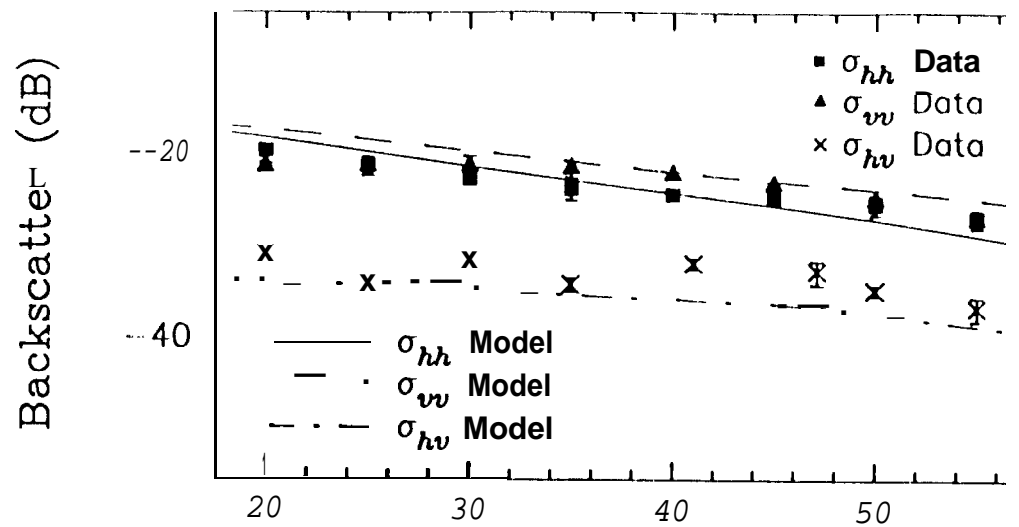


FIGURE 11

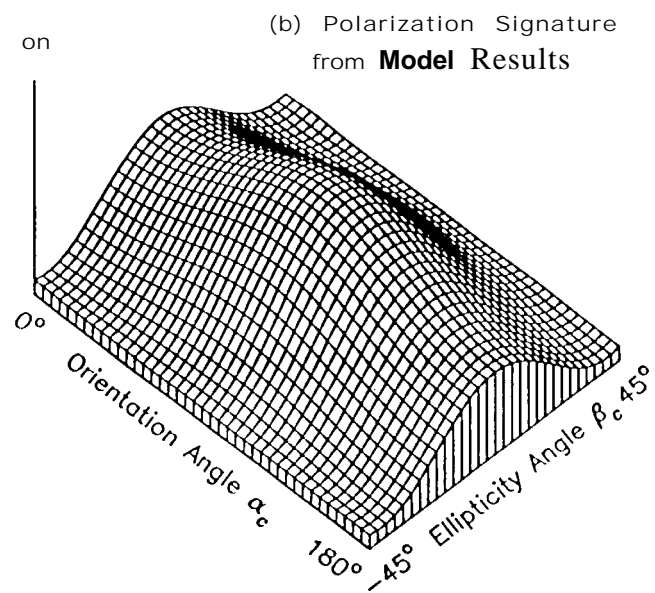
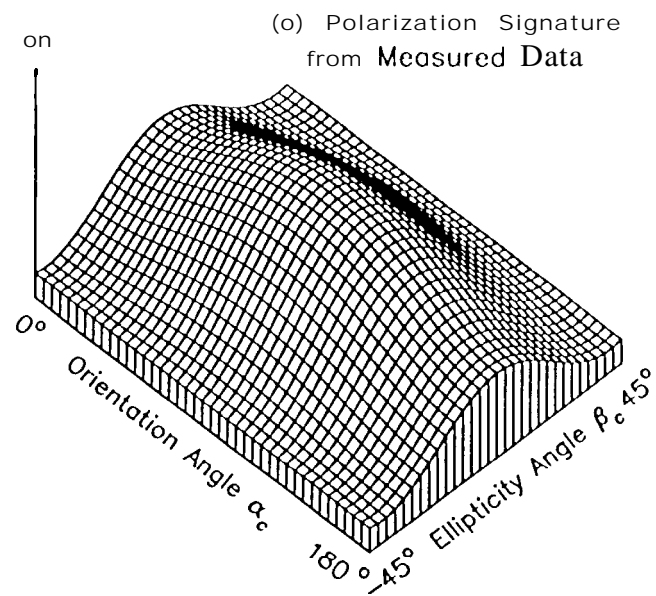


FIGURE 12

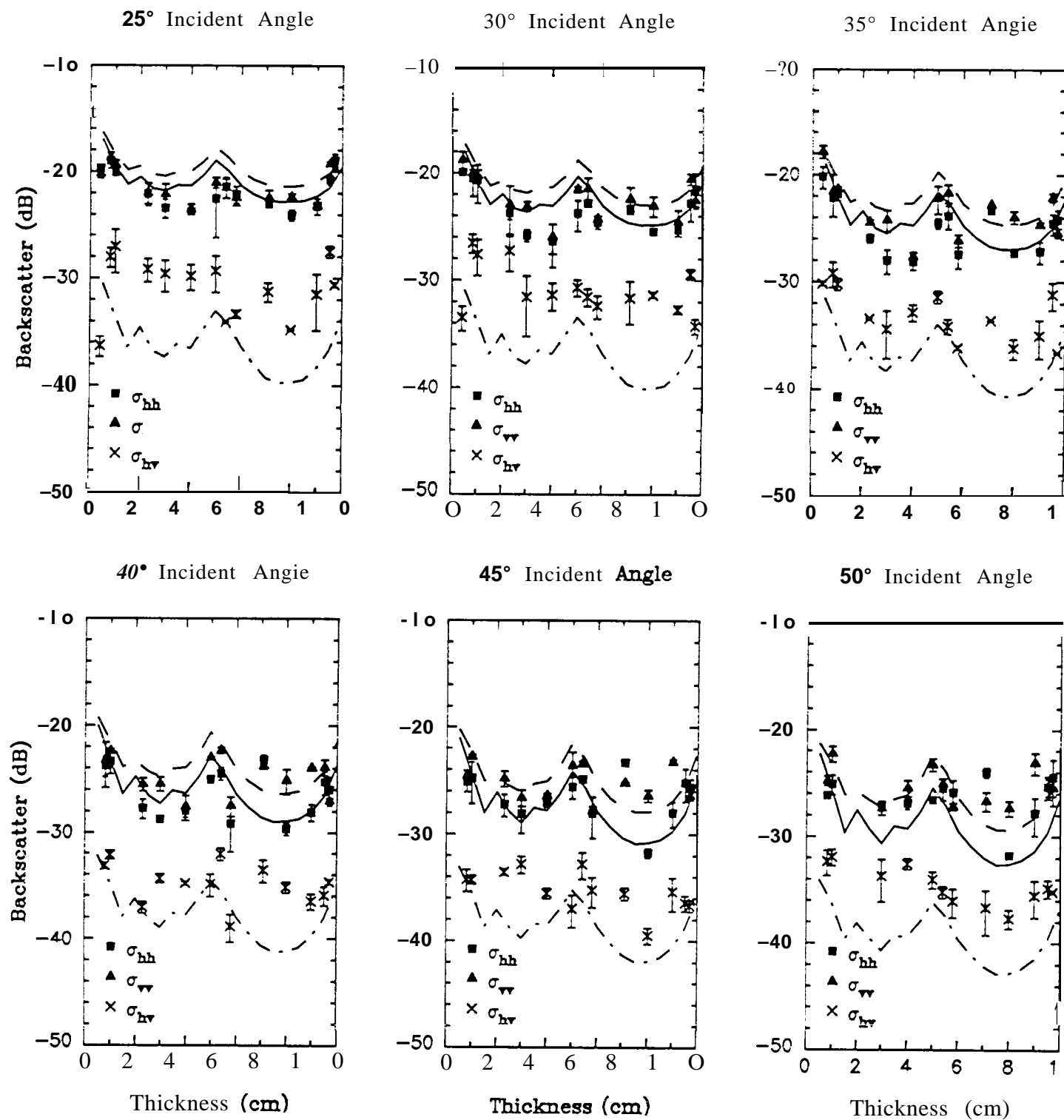


FIGURE 13

Salt Type	Chemical Representation	Mixing Portion (kg . m ⁻³)
Sodium Chloride	NaCl	24.0
Magnesium Chloride	MgCl ₂	3.27
Magnesium Sulfate	MgSO ₄	1.50
Calcium Sulfate	case,	1.10
Potassium Sulfate	K ₂ SO ₄	0.698
(Lithium) Carbonate	CaCO ₃	0.104

Table 1. Salt composition of sea water used in this experiment.